arXiv:1110.6420v2 [astro-ph.SR] 7 Nov 2011

Imaging with *HST* the time evolution of Eta Carinae's colliding winds [1]

Theodore R. Gull
Code 667, Astrophysics Science Division, Goddard Space Flight Center, Greenbelt, MD 20771, USA; Theodore.R.Gull@nasa.gov

Thomas I. Madura and Jose H. Groh
Max-Planck-Institut fur Radioastronomie, Auf dem Hugel 69, D-53121 Bonn, Germany
and

Michael F. Corcoran[2]
CRESST and X-ray Astrophysics Laboratory, Goddard Space Flight Center, Greenbelt, MD 20771, USA

ABSTRACT

We report new *HST*/STIS observations that map the high-ionization forbidden line emission in the inner arcsecond of Eta Car, the first that fully image the extended wind-wind interaction region of the massive colliding wind binary. These observations were obtained after the 2009.0 periastron at orbital phases 0.084, 0.163, and 0.323 of the 5.54-year spectroscopic cycle. We analyze the variations in brightness and morphology of the emission, and find that blue-shifted emission (-400 to -200 km s^{-1}) is symmetric and elongated along the northeast-southwest axis, while the red-shifted emission ($+100$ to $+200$ km s^{-1}) is asymmetric and extends to the north-northwest. Comparison to synthetic images generated from a 3-D dynamical model strengthens the 3-D orbital orientation found by Madura et al. (2011), with an inclination $i \approx 138°$, argument of periapsis $\omega \approx 270°$, and an orbital axis that is aligned at the same PA on the sky as the symmetry axis of the Homunculus, 312°. We discuss the potential that these and future mappings have for constraining the stellar parameters of the companion star and the long-term variability of the system.

Subject headings: stars: atmospheres — stars: mass-loss — stars: winds, outflows — stars: variables: general — supergiants — stars: individual (Eta Carinae)

1. Introduction

Eta Carinae, one of the most luminous, variable objects in our Milky Way, is sufficiently close ($D = 2.3 \pm 0.1$ kpc, Smith 2006) that we can study many of its properties throughout the electromagnetic spectrum. As noticed by Damineli (1996), the object exhibits a 5.54-year orbital period characterized by a lengthy high ionization[1] state with multiple high ionization forbidden lines that disappear during months-long low ionization state (Damineli et al. 2008b). Eta Car is considered to be a massive, highly eccentric ($e \sim 0.9$,

[1]Support for program 12013 was provided by NASA through a grant from the Space Telescope Science Institute, which is operated by the Association of Universities for Research in Astronomy, Inc., under NASA contract NAS 5-26555.

[2]Universities Space Research Association, 10211 Wincopin Circle, Ste 500, Columbia, MD 21044

[1]Low and high ionization are used here to describe atomic species with ionization potentials (IPs) below and above 13.6 eV, the IP of hydrogen.

Corcoran 2005; Nielsen et al. 2005) binary consisting of η_A, a luminous blue variable (LBV), and η_B, a hot, less massive companion not directly seen, but whose properties have been inferred from its effects on the wind of η_A and the photoionization of nearby ejecta (Verner et al. 2005; Teodoro et al. 2008; Mehner et al. 2010, hereafter Me10; Groh et al. 2010a,b)

The total luminosity, dominated by η_A, is $\geq 5\times10^6$ $L_\odot$ (Davidson & Humphreys 1997), with the total mass of the binary exceeding 120 $M_\odot$ (Hillier et al. 2001, hereafter H01). Radiative transfer modeling of *HST*/STIS spatially-resolved spectroscopic observations suggests that η_A has a mass $\gtrsim 90\ M_\odot$, and a stellar wind with a mass-loss rate of $\sim 10^{-3} M_\odot$ yr^{-1} and terminal speed of $\sim 500-600$ km s^{-1} (Hillier et al. 2001; Hillier et al. 2006, hereafter H06). Models of the observed X-ray spectrum require the wind terminal velocity of η_B to be ~ 3000 km s^{-1} with a mass-loss rate of $\sim 10^{-5} M_\odot$ yr^{-1} (Pittard & Corcoran 2002). The spectral type of η_B has been loosely constrained via modeling of the inner ejecta to be a mid-O supergiant (Verner et al. 2005; Teodoro et al. 2008; Me10).

3-D numerical simulations suggest that the wind of η_B strongly influences the very dense wind of η_A, creating a low-density cavity and *inner* wind-wind collision zone (WWCZ) (Pittard & Corcoran 2002; Okazaki et al. 2008; Parkin et al. 2009). The geometry and physical conditions of this inner region have been constrained from spatially unresolved X-ray (Henley et al. 2008), optical (Nielsen et al. 2007; Damineli et al. 2008a), and near-infrared (Groh et al. 2010a,b) observations.

In addition to the interaction between the two winds in the inner region (at spatial scales comparable to the semi-major axis length, $a \approx 15.4$ AU $= 0\farcs0067$ at 2.3 kpc), the 3-D hydrodynamical simulations predict an *outer, extended*, ballistic WWCZ that stretches to distances several orders of magnitude larger than the size of the orbit (Okazaki et al. 2008; Madura 2010, hereafter M10). Observational evidence for an extended WWCZ comes from the analysis of previous *HST*/STIS longslit observations (G09; M10; Madura et al. 2011, hereafter M11) which revealed spatially-extended forbidden line emission from low- and high-ionization species at $\sim 0\farcs1$ to $0\farcs7$ (230 to 1600 AU) from the central core. During the high state, [Fe II] line emission extends up to ±500 km s^{-1} along the STIS slit, while [Fe III] line emission extends to -400 km s^{-1} for STIS slit position angles close to 45°. Radiative transfer modeling of the extended [Fe III] emission (M10; M11) tightly constrains the orbital inclination, $i \approx 138°$, close to the axis of inclination of the Homunculus, and the argument of periapsis $240° \lesssim \omega \lesssim 270°$ in agreement with most researchers (Damineli et al. 2008b; Groh et al. 2010a; Parkin et al. 2009 and references therein). This constraint invalidates the claim by several groups (Falceta-Gonçalves & Abraham 2009; Kashi & Soker 2009 and references therein) that periastron occurs on the near side of η_A ($\omega = 90°$).

Here we report new *HST*/STIS observations, the first that fully map the inner arcsecond high-ionization, forbidden line emission of Eta Car. Maps of [Fe III] $\lambda\lambda$4659.35, 4702.85[2] and [N II] λ5756.19 recorded in early phases following the 2009.0 periastron event show changes in the wind structures excited by FUV radiation from η_B. These results demonstrate that structural changes can be followed using specific forbidden lines, leading to increased knowledge about interacting wind properties, the parameters of the binary orbit and, most importantly, the stellar properties of η_B.

2. Observations

The *HST*/STIS mapping observations were obtained after the successful repair of STIS during Service Mission 4. The first visit occurred in June 2009 ($\phi = 12.084$[3]) as an early release observation demonstrating the repaired-STIS capabilities (Program 11506 PI=Noll). The second and third visits were scheduled in December 2009 ($\phi = 12.163$) and October 2010 ($\phi = 12.323$) under a CHANDRA/*HST* grant (Program 12013, PI Corcoran).

All observations were performed with the $52'' \times 0\farcs1$ longslit. The strongest, most isolated, high-ionization forbidden emission lines from the inner and outer WWCZs are [Fe III] $\lambda\lambda$ 4659, 4702 and

[2]All wavelengths are measured in vacuum.

[3]All observations are referenced by cycle number relative to cycle 1 beginning 1948 February, following the convention introduced by Groh & Damineli (2004). The phase ϕ is zeroed to JD2482819.8 $\pm$ 0.5 with period $P = 2022.7 \pm 1.3$ days (Damineli et al. 2008b).

[N II] λ5756 (G09). The STIS gratings, G430M, centered at λ4706, and G750M, centered at λ5734, provide a spectral resolving power of about 8000.

Spatial mapping was accomplished with the standard STIS-PERP-TO-SLIT mosaic routine using the $52'' \times 0''.1$ aperture with multiple $0''.1$ offset position spacings centered on Eta Carinae. The size of the map, given limited foreknowledge of the extended forbidden emission structure, was adjusted with each visit based upon the anticipated *HST*/STIS longslit position angle (PA), pre-determined by the *HST* solar panel orientation. As buffer dumps impact the total integration time, only the central CCD rows, typically 64 ($3''.2$) or 128 ($6''.4$), were read out. The PAs for each visit were PA = $79°(\phi = 12.084)$, -121°($\phi = 12.163$), and -167°($\phi = 12.323$). Since a full spatial map was obtained during each visit, the PA has little effect on the results presented here (see Figures 1 and 2).

The data were reduced with STIS GTO CALSTIS software. While data quality is similar to previous *HST*/STIS observations of Eta Car obtained from 1998 to 2004 (Davidson et al. 2005; G09), the CCD detector has increased number of hot pixels, some bad columns, and increased charge transfer inefficiencies. Bright local continuum (Figure 1b) was subtracted from each pixel, isolating the faint forbidden line emission (Figures 1c-i, 2). Velocity channels were co-added to produce blue (-400 to -200 km s^{-1}), low-velocity (-90 to $+30$ km s^{-1}), and red ($+100$ to $+200$ km s^{-1}) images for each of the high-ionization forbidden lines (Figure 2). Only the high velocity blue and red maps are sensitive to the wind wind interaction that we model in this present work. The low velocity maps are dominated by slow-moving, extended ejecta produced in the 19th century eruptions, and so are not discussed in detail here. A refinement to the current model will include a screen of condensations to account for the low-velocity emission.

3. Results

3.1. Morphology and time evolution of the extended wind-wind collision

For each phase, we compared velocity-separated images of [Fe III] $\lambda\lambda$4659, 4702 and [N II] λ5756, and found remarkable similarities in the blue and red images between the three emission lines (see Figure 1 for June 2009, ϕ =12.084). Hereafter we focus on the [Fe III] λ4659 emission, which cannot be formed by the primary star alone. Emission of [Fe III] requires 16.2 eV photons from η_B, plus thermal collisions at electron densities approaching $N_e = 10^7$ cm^{-3} (G09; M10; M11). By comparison, [N II] emission is produced by 14.6 eV photons at electron densities approaching $N_e = 3\times10^7$ cm^{-3}. As the primary star, η_A, produces significant numbers of 14.6 eV photons (H01), [N II] emission does not fully disappear during periastron (Damineli et al. 2008a; G09). However, the red emission from [Fe III] λ4659.35 can be contaminated by blue emission from [Fe II] λ4665.75. Likewise, the red emission image of [Fe III] λ4702.85 may be depressed by He I λ4714.47 absorption. Hence, we examined the [N II] maps to ensure little or no red high-ionization emission is present.

Figure 2 shows the time evolution of the blue, low-velocity, and red components of [Fe III] λ4659 at orbital phases $\phi = 12.084$, 12.163, and 12.323. The morphology and geometry of the extended [Fe III] λ4659 emission resolved by *HST*/STIS changes conspicuously as a function of velocity and time. The blue emission extends along the NE–SW direction, along PA $\simeq 45°$, which is similar to what has been suggested from previous sparse HST/STIS long-slit observations obtained at different orbital phases across cycle 11 (G09, Me10, M10, M11). At ϕ =12.084, the linear structure is nearly symmetrical about the central region, but at later phases becomes more diffuse, shifting to the S and SE. The red emission is fuzzier, asymmetric and extends primarily to the NNW at each phase. In contrast, the low-velocity structure is larger and extends diffusely northward. The low-velocity emission is heavily dominated by emission from the Weigelt blobs (Weigelt & Ebersberger 1986) and a screen of fainter condensations (Me10), located within the η_B wind-blown cavity and thusly obscuring the much fainter WWCZ contributions. While we describe the qualitative changes of the low-velocity component, we defer the detailed modeling of this equatorial emission to a future paper.

For discussion purposes, we now isolate the central core (inner $0''.3\times0''.3$) as representative of the inner WWCZ, and a time-variant extended

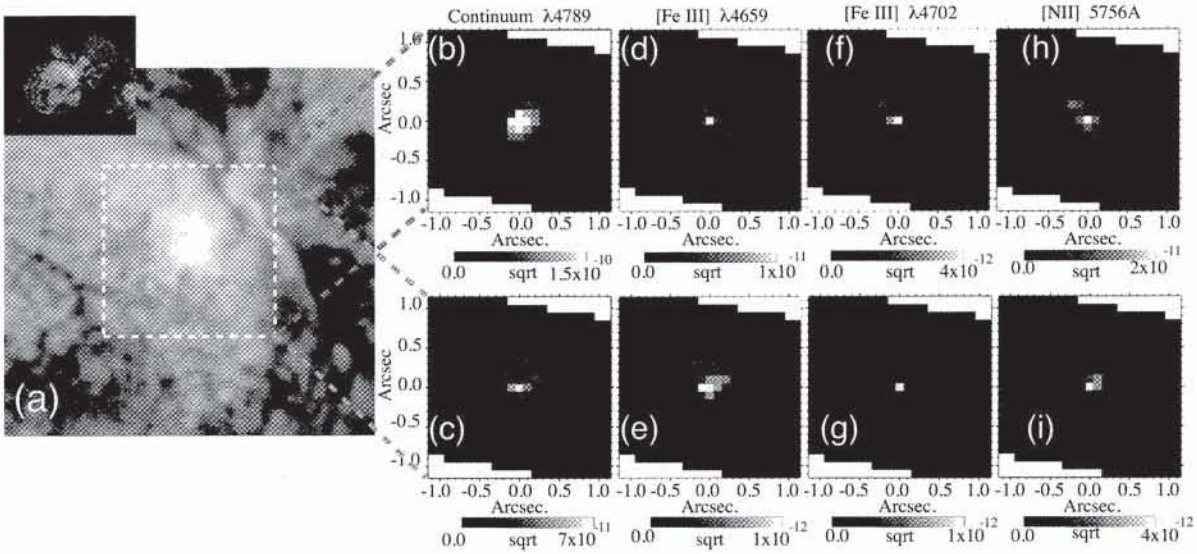

Fig. 1.— Comparison of red and blue images for isolated high-ionization forbidden lines from the ϕ =12.084 observations (June 2009). (a) *HST*/ACS image shows the 2.″2×2.″2 box centered on Eta Carinae located within the 18″ Homunculus as indicated in the small inset (HST archives). Strong continuum (b) has been subtracted from each forbidden emission map. [Fe III] λ4659 emission (c), integrated from −400 to +200 km s^{-1}, has a very different spatial distribution from the continuum. Blue images, extracted from −400 to −200 km s^{-1} for [Fe III] λ4659 (d), λ4702 (f) and [N II] λ5756 (h) are similar for each ion, as are red images extracted from +100 to +200 km s^{-1} for [Fe III] λ4659 (e), λ4702 (g) and [N II] λ5756 (i). Images are displayed as sqrt(ergs cm^{-2} s^{-1}). North is up, and east is left.

(>0.″3×0.″3) structure as representative of the outer WWCZ. These two regions have very different physical drivers. The central core exhibits X-ray (Pittard & Corcoran 2002) and He I emission, along with strong forbidden line emission. The outer WWCZ, expanding ballistically, is best traced by strong forbidden line emission. The spatially-extended blue and red emission components are thought to arise in the outer WWCZ of Eta Car (G09), composed of material which was earlier part of the inner WWCZ, but over the past 5.5-year period streamed outward (M10; M11). While the primary wind is estimated to have a terminal velocity of 500 − 600 km s^{-1}, the peak radial velocity component of the forbidden emission lines appears to be ∼ 400 km s^{-1}. At terminal velocity, the outer WWCZ expands at 0.″25 per 5.5-year cycle, hence the current WWCZ, even at ϕ =0.323, is within the 0.″3×0.″3 core.

Both the central and extended structures brighten with phase, but they change differently. At ϕ =12.084, the central core accounts for 1/3 of the flux, but brightens only thirty percent by ϕ =12.323. The extended emission more than doubles in brightness by ϕ =12.323. Brightening of the velocity components within the core and extended structures are likewise different. The brightness of the red component is nearly constant for both the core and the extended structure. The core blue component increases by seventy percent while the extended blue component doubles in brightness. The core low-velocity component increases only by fifty percent, but the low-velocity extended component triples in brightness and appears to shift further outward from the core. We note that between ϕ = 12.163 and 12.323 the brightest low-velocity component shifts from the vicinity of Weigelt C, noted by Me10, to Weigelt B and D.

These brightness changes in the core and extended structures support a scenario in which the current WWCZ, namely the direct collision be-

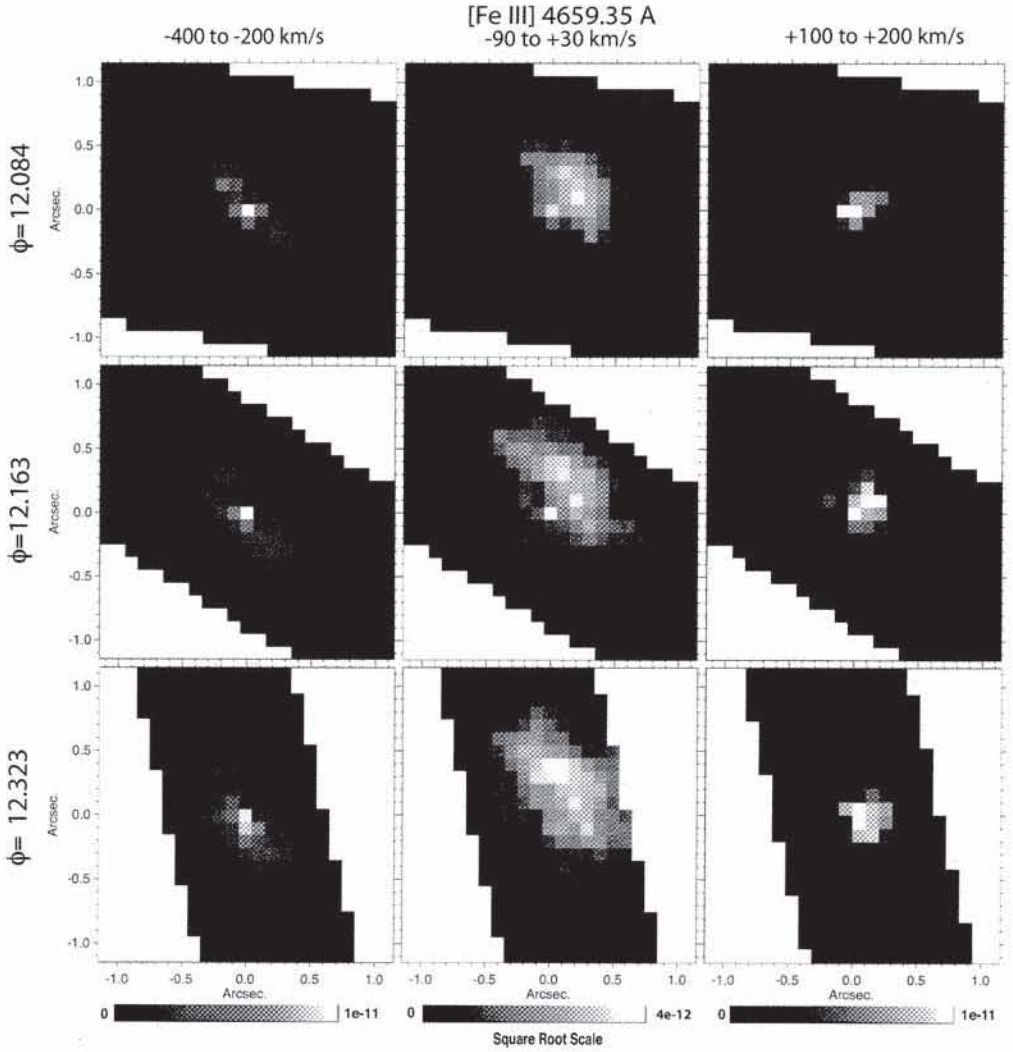

Fig. 2.— The changing shape of high-ionization [Fe III] λ4659 early in Eta Carinae's binary period. Top row: ϕ =12.084. Middle row: ϕ =12.163. Bottom row: ϕ =12.323. Left column: blue emission (-400 to -200 km s^{-1}). Middle column: low-velocity emission (-90 to $+30$ km s^{-1}). Right column: red emission ($+100$ to $+200$ km s^{-1}). Gaps between the velocity intervals are purposefully excluded to show very separate velocity fields. The color bars show flux scaled by sqrt(ergs cm^{-2}s^{-1}.)

tween the winds of η_A and η_B, is contained within the 0.″3 diameter core. After each periastron passage, a new secondary-wind-blown cavity must form and expand outward. The cavity rapidly approaches a balance between the FUV flux of η_B and the cavity wall structure at critical density. However, the outer cavity wall is very thin, ionizes rapidly and drops in density allowing FUV radiation to pass outward into the much larger, ballistically expanding outer cavity formed in the previous cycle. Within this cavity, the FUV photons encounter dense walls of primary wind. The growth in brightness in the blue images, with little change in the red images, indicates expansion in the general direction of the observer. The larger increase in brightness of the low-velocity images shows where the FUV radiation escapes through the multiple cavities built up by the wind of η_B over many cycles.

3.2. Comparison with a 3-D Dynamical Model

Proper interpretation of the mapping observations requires a full 3-D dynamical model that accounts for the effects of orbital motion on the WWCZ. Here we use full 3-D Smoothed Particle Hydrodynamics (SPH) simulations of Eta Car's colliding winds and radiative transfer codes to compute the intensity in the [Fe III] λ4659 line projected on the sky for a specified orbital orientation (M10; M11). The numerical simulations were performed using the same 3-D SPH code as that in Okazaki et al. (2008) with identical parameters except for the mass loss rate of η_A, which we changed to 10^{-3} $M_\odot$ yr^{-1} (H01; H06). The two stellar winds in our simulation are also taken to be adiabatic. In order to allow for a more direct comparison to the *HST* observations, the computational domain is a factor of ten larger than that of Okazaki et al. (2008) (i.e. $\pm$ 1600 AU $\approx \pm$ 0.″7). Details on the radiative transfer calculations can be found in M10, M11.

Figures 3 and 4 compare the observed blue and red images at ϕ = 12.163 and 12.323 with those predicted by the model for the same velocity intervals. For simplicity, the zero reference phase of the spectroscopic cycle (Damineli et al. 2008a), is assumed to coincide with the zero reference phase of the orbital cycle (i.e. periastron passage) in the 3-D SPH simulation. In a highly-eccentric binary system like Eta Car, the two values should be within a few weeks, which will not affect the overall conclusions (Groh et al. 2010b). The binary orbit is assumed to be oriented with an inclination $i = 138°$, argument of periapsis $\omega = 270°$, and an orbital axis that is aligned at the same PA on the sky as the symmetry axis of the Homunculus, 312° (Davidson et al. 2001)[4].

The relatively compact central core produces little [Fe III] emission as densities in the WWCZ walls greatly exceed the critical density for efficient emission. The low-velocity maps, displayed on a flux scale similar to the scales for the blue and red images, would be blank while the observed low velocity emission, heavily dominated by flux from the Weigelt blobs and fainter slow-moving clumps, extends to the northwest. As mentioned in section 3.1, we are refining the model to include such a screen, which will be a topic in a much more encompassing paper. Hence only the red and blue components, successfully replicated in this study, are presented in Figures 3 and 4.

The spatial extent of the emission compares quite favorably between the observations and the models (Figures 3 and 4), with the blue structures extending projected distances of $\sim 1''$ (2300 AU) along PA $\sim 45°$, and the red structures displaced to the NE of the core by $\sim$ 0.″1 to 0.″4 (230 to 1000 AU). We display unreddened fluxes for the model structures due to known uncertainties of reddening. Model fluxes, reddened by $\approx$5–20 using typical *interstellar* reddening values for stars in the vicinity of Eta Car (H01; Me10) agree with the observations within a factor of a few. This discrepancy could arise due to uncertainties in the assumed stellar parameters of both stars, the reddening law and atomic physics, or systematics in the radiative transfer and hydrodynamical modeling. However, reddening is highly variable across the Carinae complex. Moreover, reddening by dust in the Homunculus and within the extended core of Eta Car may change on very small scales. Hence we chose to display unreddened model fluxes in Figures 3 and 4.

[4]Davidson et al. (2001) determined the Homunculus axis of symmetry to be tilted 42° into the sky plane. We refer the reader to M11 for detailed discussion of the binary orbital inclination at 138°=180°-42°.

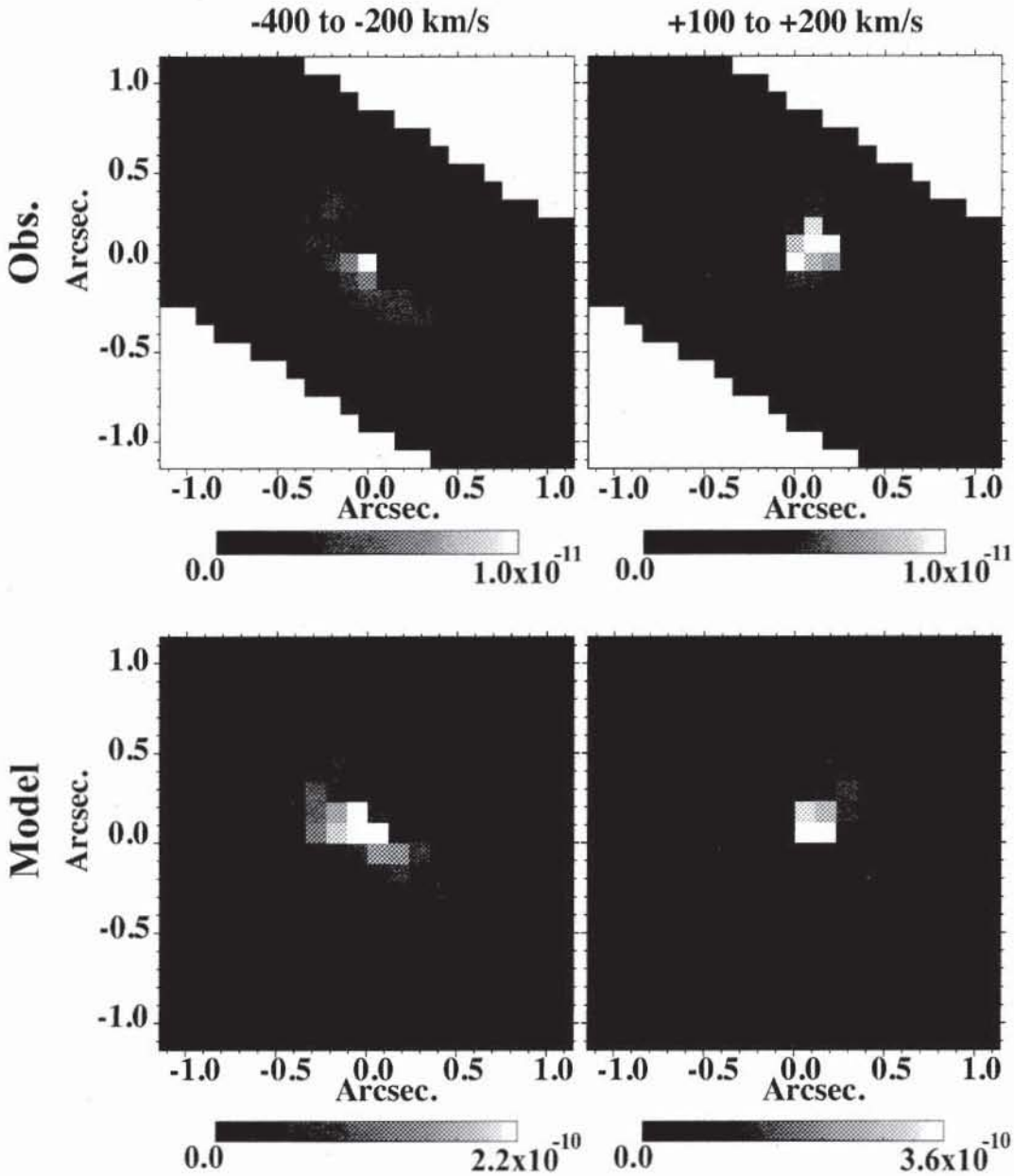

Fig. 3.— Comparison of ϕ =12.163 blue and red components to 3-D dynamical model. Top row: Observed blue and red images. Bottom Row: 3-D SPH/radiative transfer images. Left column: -400 to -200 km s^{-1}. Right column: $+100$ to $+200$ km s^{-1}. Color display in all images is on a square root scale of ergs cm^{-2} s^{-1}. North is up.

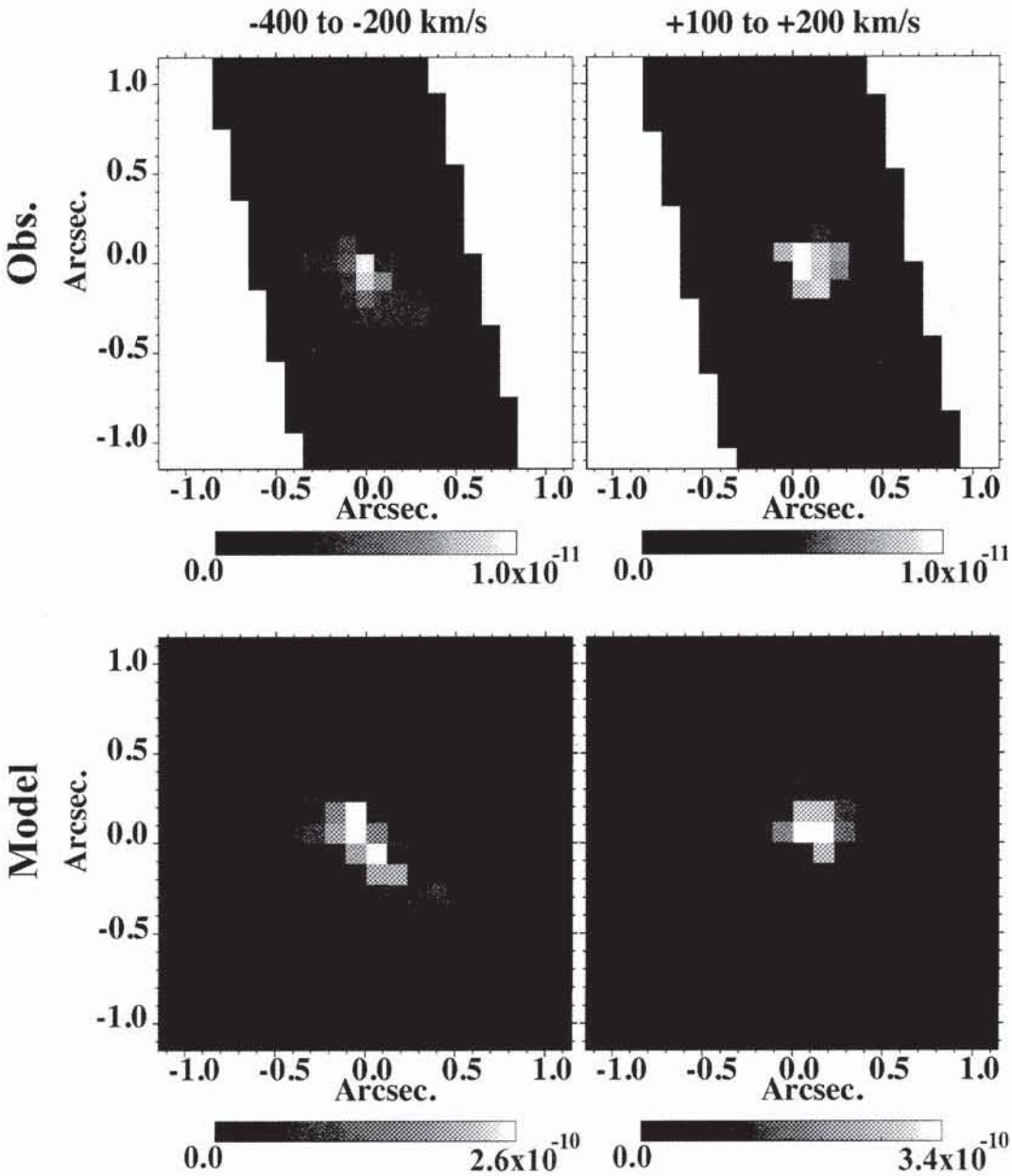

Fig. 4.— Comparison of $\phi = 12.323$ blue and red components to 3-D dynamical model as in Figure 3. Changes are subtle as η_B physically is close to the position of apastron; the ionization structure is primarily expanding.

4. Discussion

This work represents the first time the extended WWCZ of a massive colliding wind binary system has been imaged using high-ionization forbidden emission lines. Spatial- and velocity-extended emission, recorded by individual *HST*/STIS longslit observations at various phases and PAs, provided impetus to expand 3-D models to simulate the wind dynamics leading to this emission. Indeed, the initial 3-D dynamical model above produces red and blue images that are similar to those observed. From multiple longslit observations, G09, M10 and M11 demonstrated that the binary orbit could be fully constrained in 3-D. The noticeable symmetry in velocity for observations taken at PA=38° (G09) is now reinforced by the spatial symmetry about the central core in the blue maps. Our modeling, of the observed maps suggests that the argument of periapsis must be closer to ω =270° than 240°, thus further reinforcing the result that η_B is on the near side of η_A at apastron, with periastron passage on the far side (Damineli et al. 1997; Pittard & Corcoran 2002; Okazaki et al. 2008; Parkin et al. 2009; G09, M10; M11).

These and future spatial maps of Eta Car's high-ionization forbidden emission have the potential to determine the nature of the unseen companion star η_B. The mass-loss rate of η_A and ionizing flux of photons from η_B determine which regions of Eta Car's WWCZ are photoionized and capable of producing high-ionization forbidden line emission like the forbidden emission from Fe^{++}, due to 16.2 eV radiation. Comparing this mass model loss rates and UV fluxes to those of stellar models for a range of O (Martins et al. 2005; Me10) and WR (Crowther 2007) stars would allow one to obtain a luminosity and temperature for η_B. Both the current model (M10; M11) and previous individual *HST*/STIS longslit observations (G09) show major changes with orbital phase, especially near periastron. Mappings at multiple phases around periastron are therefore essential in order to determine when the FUV radiation from η_B becomes trapped in the dense wind of η_A and the extended high-ionization emission vanishes, and likewise when η_B emerges from η_A's wind and the extended emission returns.

This approach has a number of advantages over previous 1-D modeling efforts to constrain η_B's properties (Verner et al. 2005; Me10), which probe the ionization structure of the Weigelt blobs. Such 1-D models make considerable assumptions about the physical conditions within the blobs and intervening material, leading to poor constraints on the luminosity of η_B.

Eta Car is variable, not only on a 5.5-year period, but has a centuries-long history of variation, including two major eruptions (Davidson & Humphreys 1997; Humphreys et al. 2008; Smith & Frew 2010). These high-ionization forbidden emission lines are powerful tools for monitoring changes in the WWCZ, providing quantitative information on the properties of the individual binary components and changes thereof, including a historical record of the recent decade-long mass loss from the primary. Following this system will provide unique information on how a massive star, during the LBV stage, loses much of its mass on its way to becoming a supernova.

We sincerely thank G. Weigelt, S. Owocki, A. Damineli and A. Okazaki for many fruitful discussions and encouragements. TG acknowledges the hospitality of MPIR during his multiple visits. We thank the referee for insightful comments leading to an improved presentation.

REFERENCES

Corcoran, M. F. 2005, AJ, 129, 2018

Crowther, P. A. 2007, ARA&A, 45, 177

Damineli, A. 1996, ApJL, 460, L49

Damineli, A., Conti, P. S., & Lopes, D. F. 1997, New Astronomy, 2, 107

Damineli, A., Hillier, D. J., Corcoran, M. F., et al. 2008a, MNRAS, 386, 2330

Damineli, A., Hillier, D. J., Corcoran, M. F., et al. 2008b, MNRAS, 384, 1649

Davidson, K. and Humphreys, R.M. 1997, ARA&A, 35, 1

Davidson, K., Martin, J., Humphreys, R. M., et al. 2005, AJ, 129, 900

Davidson, K., Smith, N., Gull, T. R., Ishibashi, K., & Hillier, D. J. 2001, AJ, 121, 1569

Falceta-Gonçalves, D., & Abraham, Z. 2009, MNRAS, 399, 1441

Groh, J. H., & Damineli, A. 2004, Information Bulletin on Variable Stars, 5492, 1

Groh, J. H., Madura, T. I., Owocki, S. P., Hillier, D. J., & Weigelt, G. 2010a, ApJ, 716, L223

Groh, J. H., Nielsen, K. E., Damineli, A., et al. 2010b, A&A, 517, A9+

Gull, T. R., Nielsen, K. E., Corcoran, M. F., et al. 2009, MNRAS, 396, 1308 (G09)

Henley, D. B., Corcoran, M. F., Pittard, J. M., et al. 2008, ApJ, 680, 705

Hillier, D. J., Davidson, K., Ishibashi, K., & Gull, T. 2001, ApJ, 553, 837 (H01)

Hillier, D. J., Gull, T., Nielsen, K., et al. 2006, ApJ, 642, 1098 (H06)

Humphreys, R. M., Davidson, K., & Koppelman, M. 2008, AJ, 135, 1249

Kashi, A., & Soker, N. 2009, MNRAS, 397, 1426

Madura, T. I. 2010, PhD thesis, University of Delaware (M10)

Madura, T. I., Gull, T. R., Owock, S. P., Groh, J. H., Okazaki, A. T., & Russell, C. M. P. 2011b, MNRAS, submitted (M11)

Martins, F., Schaerer, D., and Hillier, D. J. 2005, A&A, 436, 1049

Mehner, A., Davidson, K., Ferland, G. J., & Humphreys, R. M. 2010, ApJ, 710, 729 (Me10)

Nielsen, K. E., Corcoran, M. F., Gull, T. R., et al. 2007, ApJ, 660, 669

Nielsen, K. E., Gull, T. R., & Vieira Kober, G. 2005, ApJS, 157, 138

Okazaki, A. T., Owocki, S. P., Russell, C. M. P., & Corcoran, M. F. 2008, MNRAS, 388, L39

Parkin, E. R., Pittard, J. M., Corcoran, M. F., Hamaguchi, K., & Stevens, I. R. 2009, MNRAS, 394, 1758

Pittard, J. M. & Corcoran, M. F. 2002, A&A, 383, 636

Smith, N. and Frew, D. J. 2010, arXiv:1010.3719

Smith, N. 2006, ApJ, 644, 1151

Teodoro, M., Damineli, A., Sharp, R. G., Groh, J. H., & Barbosa, C. L. 2008, MNRAS, 387, 564

Verner, E., Bruhweiler, F., & Gull, T. 2005, ApJ, 624, 973

Weigelt, G. & Ebersberger, J. 1986, A&A, 163, L5

This 2-column preprint was prepared with the AAS LaTeX macros v5.2.